PAPER

Disconnection of scrape off layer turbulence between the outer midplane and divertor target plate in NSTX

To cite this article: F. Scotti *et al* 2020 *Nucl. Fusion* **60** 026004

View the article online for updates and enhancements.

Recent citations

- A new mechanism for filament disconnection at the X-point: poloidal shear in radial E × B velocity
F. Nespoli *et al*

Disconnection of scrape off layer turbulence between the outer midplane and divertor target plate in NSTX

F. Scotti[1], **S. Zweben**[2], **J. Myra**[3], **R. Maqueda**[4] **and V. Soukhanovskii**[1]

[1] Lawrence Livermore National Laboratory, Livermore, CA 94550, United States of America
[2] Princeton Plasma Physics Laboratory, Princeton, NJ 08540, United States of America
[3] Lodestar Research Corporation, Boulder, CO 80301, United States of America
[4] X Science LLC, Plainsboro, NJ 08536, United States of America

E-mail: fscotti@pppl.gov

CrossMark

Abstract

The connection between scrape off layer (SOL) turbulence at the outer midplane and at the divertor target plate is characterized in the National Spherical Torus Experiment (NSTX). Divertor fluctuations due to midplane blobs are studied by imaging their helical intersection with the divertor plate. Divertor fluctuation levels gradually decrease approaching the outer strike point. Divertor radial turbulence scale lengths as well as radial and poloidal turbulence propagation velocities are comparable to those on the low field side midplane. Strong correlation between divertor and midplane turbulence is observed in the far SOL. The correlation progressively decreases towards the separatrix, along with the decrease in the measured divertor fluctuations. The reduction in correlation is consistent with an electrostatic two-region blob model (Myra *et al* 2006 *Phys. Plasmas* **13** 112502) with perpendicular ion polarization currents due to X-point geometry causing filament disconnection.

Keywords: plasma, scrape-off layer, divertor, turbulence, NSTX

(Some figures may appear in colour only in the online journal)

1. Introduction

Narrow scrape-off layer (SOL) heat flux profiles and particle fluxes to the first wall are two of the concerns for the survivability of wall materials in future fusion reactors. Extrapolation from present tokamaks indicates that the expected narrow heat flux features in the near SOL of ITER will result in unacceptable (if unmitigated) divertor peak heat fluxes [2, 3]. At the same time, particle fluxes due to charge-exchange neutrals and intermittent plasma transport could limit first wall lifetime due to erosion, while producing unacceptable amounts of dust [4]. In order to validate the extrapolation from measurements in current devices, a systematic understanding of the mechanisms (turbulent and neoclassical transport) responsible for setting the radial heat and particle flux profiles is needed.

SOL turbulence due to mesoscale structures, called blobs or filaments and generated on the low field side (LFS) midplane

by interchange or drift wave instabilities, has been extensively studied in diverted toroidally confined devices (NSTX [5, 6], MAST [7, 8], DIII-D [9, 10], C-Mod [11], TCV [12], ASDEX-Upgrade [13], JT-60U [14]). Intermittent plasma objects were shown to be responsible for a large fraction of the SOL particle fluxes (e.g. up to 50% in DIII-D [15]). Recently, experiments have begun to study the parallel structure of SOL turbulence such as, for example, its connection to the divertor target plate. Meanwhile, additional types of localized divertor region turbulence have also been discovered which do not connect along field lines to the outer midplane (see below).

In recent years, several tokamaks have studied turbulent fluctuations in the divertor region. Divertor fluctuations were measured with reciprocating and target-mounted probes in MAST [16], ASDEX-Upgrade [17] and JT-60U [14], showing an increase in intermittency moving radially outwards in the SOL in MAST and JT-60U. In NSTX [18], the 3D filament

intersection with the divertor target plate was identified as the parallel extension of midplane blobs, and a large parallel cross-correlation was found between midplane and divertor turbulence in the far SOL. In Alcator C-Mod, filaments were imaged near the X-point region, showing elongated fluctuating structures consistent with field-line mapping from blobs at the outer midplane [19], and a high cross-correlation was found between SOL fluctuations measured at the midplane using GPI and probes at the X-point and divertor target plate [20]. In the COMPASS tokamak, correlation up to 0.4 was found between midplane filaments measured with passive imaging and divertor target Langmuir probes [21]. Divertor-localized modes were observed near the separatrix on the outer divertor leg and in the private flux region in the inner divertor leg in MAST [22], C-Mod [23] and NSTX-U [24]. Recent analysis of passive imaging of the lower divertor in MAST also identi-fied a quiescent region in proximity of the X-point [25]. The effect of an X-point on blob dynamics was studied in the Toroidal Plasma Experiment TORPEX with diverted mag-netic geometry, although not in a tokamak configuration [26].

Theoretical models have investigated the parallel structure of midplane blobs and their connection to the divertor region. The parallel filament extent was found to be affected by col-lisionality [27] and magnetic geometry in the presence of an X-point [28]. An electrostatic two region model, based on the solution of two sets of continuity and vorticity equations, was developed by Myra [1] to study the effect of collision-ality, blob size and X-point geometry on filament propaga-tion. The scaling of blob radial velocity with blob size was found to change depending on whether the parallel filament structure was limited by X-point fanning or collisionality. Changes in the filaments radial motion can then affect both the SOL width and the particle flux to the first wall. Some predictions from this model were confirmed in experiments in ASDEX-Upgrade and JET which related the formation of a density shoulder in the SOL to divertor collisionality and its role in disconnecting filaments from the divertor plate [29]. Recent work in JET [30] and TCV [31], however, has shown cases where these predictions fail, indicating that col-lisionality might not be the only cause for shoulder formation. Modeling with the ArbiTER code in NSTX geometry [32] and BOUT++ in DIII-D geometry [33] has also shown limited penetration of midplane turbulence near the outer strike point.

In summary, previous experiments have often shown a connection between outer midplane and divertor target plate turbulence in the tokamak SOL region. However, there is also some experimental evidence and theoretical justification for the possibility of a disconnection of the turbulence very near the separatrix.

The present paper is dedicated to the identification of a dis-connection region between midplane and divertor target turbu-lence near the separatrix, via a comparison between upstream and downstream turbulence properties. This paper extends previous work by Maqueda [18] with a detailed comparison of upstream and downstream spatial correlation functions and radial and poloidal dynamics across the entire divertor, from the outer strike point to the far SOL. The analysis is based on repeated L-mode discharges in NSTX and is carried out via

fast camera imaging of upstream turbulence and of the inter-section of turbulence filaments with the divertor plate. Results are discussed in the context of the blob model from [1].

The paper is organized as follows: section 2 describes experimental setup and method, section 3 introduces the appearance of midplane blobs in the divertor, sections 4 and 5 discuss divertor and midplane turbulence characterisitcs, section 6 compares midplane and divertor turbulence scale lengths and propagation, section 7 presents the correlation between midplane and divertor turbulence, sections 8 and 9 are dedicated to discussion and conclusions.

2. Experimental setup and method

This work examines the correlation between midplane and divertor target turbulence measured via fast camera imaging and Langmuir probes. Five repeated ohmically-heated L-mode discharges from the 2010 NSTX campaign are considered, with a lower single null diverted configuration ($\delta r_{sep} \sim 2$ cm), 800 kA of plasma current (I_p), Greenwald fraction $f_G \sim 0.2$– 0.3 and $B \times \nabla B$ ion drift direction towards the lower divertor. This section describes the diagnostics employed. A schematic of the diagnostics is shown in figure 1(*a*) overlaid to an NSTX equilibrium reconstruction for one of the repeated discharges (141754).

Midplane turbulence properties are evaluated with the Gas Puff Imaging diagnostic (GPI) [34]. The GPI diag-nostic images plasma filaments through deuterium Balmer α ($D - \alpha$) emission measured with a fast CMOS camera from a field aligned view on the low field side (LFS) midplane. A gas puff through an in-vessel manifold is used to *illuminate* tur-bulence structures in the LFS plasma edge, projecting the 3D filaments on a plane nearly orthogonal to the local magnetic field. The image plane defined by the gas manifold is tilted about 38° with respect to the vertical axis. A Vision Research Phantom 710 CMOS camera is used with 2 μs exposure time, 400 kHz framing rate and a 1 cm resolution in the image plane defined by the gas manifold. The projection of the field of view in the (R, Z) plane is shown in figure 1(*a*) with a green box. In the discharges analyzed in this paper, the GPI gas puff is at the start of the I_p flat-top ($t = 0.2$ s).

Divertor turbulence properties are evaluated via pas-sive imaging and Langmuir probes. The top–down view of the lower divertor, described in [35] and shown in purple in figure 1(*a*), is used to image divertor fluctuations, similarly to what was done in [18]. A Vision Research Phantom v710 fast CMOS camera provides a wide angle view of the lower divertor (covering $\sim$300° toroidally) with frame rates of 97 kHz, a crop resolution of 256×208 pixels and a spatial res-olution on the divertor target of $\sim$0.8 cm/pixel. Spatial resolu-tion was improved by $\sim$50% and framing rates were increased by $\sim$10% with respect to [18].

The divertor fast camera was filtered for neutral lithium (Li I) emission at 670.8 nm, which is the brightest visible emission line in attached divertor conditions with lithium conditioning in NSTX. The very short lithium ionization mean free path results in emission that is localized to a few
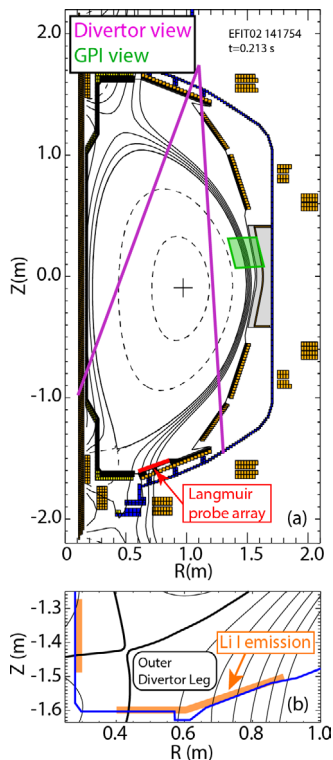
Figure 1. (*a*) NSTX equilibrium reconstruction with overlay of Langmuir probe array location (red) and camera fields of view: top–down view (purple), GPI view (green); (*b*) close-up of the divertor with schematic of Li I emission region (orange).

mm above the divertor plate. Therefore, imaging via Li I emission enables isolating the intersection (or *footprint*) of the turbulent filaments with the divertor target. A schematic of the typical extent of Li I emission is shown in orange in figure 1(*b*) overlaid to an NSTX reconstruction. As will be discussed in section 4, fluctuations in Li I brightness can be interpreted as being representative of electron density n_e fluctuations.

In order to ease the visualization and interpretation of divertor filaments, the 2D data are remapped from real space to radius and toroidal angle as discussed in [35]. For a given equilibrium reconstruction, divertor radii are mapped to flux surface coordinates and used for a direct comparison with upstream quantities.

While fast divertor imaging enables the characterization of the 2D structure of divertor turbulence, its interpretation is complicated by the non-linearity of the emissivity with respect to the fluctuating quantities n_e, T_e, n_{Li}. Langmuir probes are employed to correlate fluctuations in Li I emission with fluctuations in plasma parameters. The Langmuir probes used in this work are part of the high density langmuir probe (HDLP) array [36] located in the lower outer divertor of NSTX and composed of five triple probes digitized at 250 kHz with a probe tip of 3 mm in the radial direction.

Equilibrium reconstructions used in this work are calculated by the EFIT code ('partial kinetic' EFIT02) and are used to relate upstream (midplane) and downstream (divertor target) turbulence properties. Uncertainties in the separatrix location are typically estimated to be on the order of 1 cm.
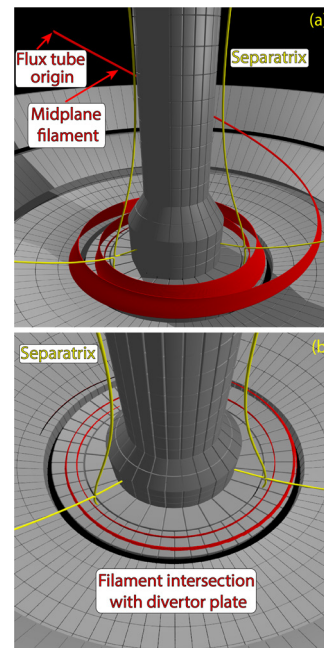
Figure 2. Rendering of a flux tube corresponding to a midplane blob in NSTX (*a*) and of its intersection with the divertor target (*b*). The separatrix is shown in yellow at two toroidal locations.

Electron temperature T_e and density n_e profiles at midplane are measured by the multi point Thomson scattering (MPTS) system [37].

3. Structure of magnetic flux tubes in the SOL

Turbulence at the low field side midplane has characteristic lengths perpendicular to the magnetic field much shorter than parallel to it, which is a consequence of the fast electron motion along field lines. Figure 2(*a*) shows the field line mapping of a circular flux tube at midplane until it intersects the divertor target plate, rendered with the ray tracing program POV-Ray [38]. Due to magnetic shear and flux expansion, the flux tube is stretched into a ribbon-like structure while it winds around the center stack. The spiral intersection of the flux tube with the divertor target is shown in figure 2(*b*) where the rendering is limited to a few mm above the divertor floor to reproduce the Li I emission and the camera is moved to a top down view to reproduce the view in the experiment.

In order to compare upstream/downstream turbulence properties and the radial extent of the turbulence connection, corresponding quantities need to be derived at the two locations (midplane and divertor) from the two camera views. This section introduces the approach used to extract divertor turbulence properties that correspond to those calculated in poloidal (binormal) and radial coordinates at midplane. This method will enable a direct comparison between upstream and downstream turbulence scale lengths and velocities in magnetically connected regions.

Figure 3(*a*) shows poloidal flux contours at the outer midplane from an EFIT02 equilibrium reconstruction for an NSTX discharge. A series of points along the radial coordinate
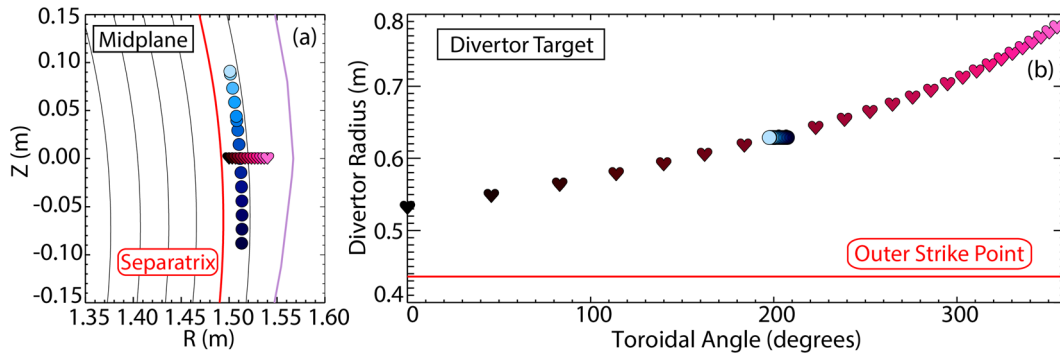
Figure 3. (*a*) Radial and poloidal coordinates at the low field side midplane; (*b*) divertor coordinates equivalent to midplane radial and poloidal coordinates.

at the outer midplane is shown with pink hearts. Points along a poloidal coordinate on a SOL flux surface are shown with blue circles. Both sets of points, at the same upstream toroidal angle, were connected to the divertor target following the field lines using the EFIT02 reconstruction. The intersection of these field lines with the divertor plate is shown in figure 3(*b*) and plotted as a function of toroidal angle and divertor radius (the outer strike point is located at $R_{div} \sim 43$ cm). The radial coordinate in the midplane field of view is represented at the divertor target as a coordinate along the spiral intersection (with radii mapping to the same normalized flux coordinates). The poloidal coordinate at midplane corresponds to a toroidal coordinate at the divertor target intersection. Therefore, a radial motion at midplane translates into a motion along the spiral while a poloidal motion at midplane corresponds to a toroidal rotation of the divertor target spiral (or, in the remapped coordinates, a toroidal translation). These observations will be used in section 6 to derive corresponding scale lengths and propagation velocities at midplane and divertor.

4. Divertor turbulence characteristics

Divertor fluctuations due to midplane blobs are observed as intermittent spirals in the lower divertor Li I emission. These spirals represent the intersection of the filaments with the divertor target plate. The appearance of midplane filaments at the divertor target in NSTX was first discussed in [18]. This section examines the characteristics of divertor turbulence while the relationship between divertor and midplane fluctuations will be presented in detail in section 7. Figure 4(*a*) shows the average Li I emission in the lower divertor. Emission is axisymmetric and peaked at the outer strike point on the divertor target and at the inner strike point on the center stack. Figure 4(*b*) shows an image of the lower divertor after a high pass filter obtained with a moving minimum subtraction. Spirals can be observed in the Li I emission in the outer divertor. Fluctuating structures are not observed in the inner divertor SOL, as expected given the stabilizing effect of curvature on the high field side. The high pass-filtered image is plotted in figure 4(*c*) as a function of toroidal angle and divertor radius.

Divertor fluctuation levels up to 40% are observed in the SOL and progressively decrease towards the separatrix. Figure 5(*a*) shows the average neutral lithium brightness at the outer strike point, plotted as a function of normalized poloidal flux ψ_N. The error bars represent the standard deviation over a 5 ms interval. Figure 5(*b*) shows the fluctuation level (standard deviation over a 5 ms interval normalized by the average count) plotted as a function of ψ_N. Different colors represent different times around the start of discharge flat-top. The fluctuation level is on the order of 30%–40% in the region that is connected to midplane, i.e. between the separatrix and the LFS limiter. A gradual decrease in fluctuation level is observed towards the outer strike point and beyond the nominal midplane limiter location. This reduction in fluctuation approaching the outer strike point is similar to the observation of a quiescent region in the proximity of the X-point in the MAST divertor [25]. Similarly to what typically observed at the LFS midplane, divertor fluctuations also have a broadband frequency spectrum.

The interpretation of the fluctuation level in Li I brightness can be complicated by non-linearities in the emissivity response to the fluctuating plasma parameters. The radial increase in density towards the strike point and the inverse dependence of the Li I photon emission coefficients on n_e however could only account for a fraction of the decrease in fluctuations near the separatrix. This effect is also counteracted by the typical increase in lithium sputtering yield at the strike point in NSTX [39] which would instead act to increase the relative fluctuation level towards the strike point. Correlation analysis and comparison of correlations scale lengths were performed in the next sections to provide a better characterization of the disconnection in the proximity of the strike point.

The intermittency of divertor fluctuations in NSTX is observed to increase moving radially outwards in the SOL. A radial increase in SOL turbulence intermittency and an agreement of the probability density function (PDF) of fluctuating quantities with a Gamma distribution have been observed on the LFS midplane in many devices [40–44] and found to be consistent with a stochastic model for SOL transport with uncorrelated exponential pulses and exponentially distributed amplitudes and waiting times [45]. Figure 6(*a*) shows the PDF
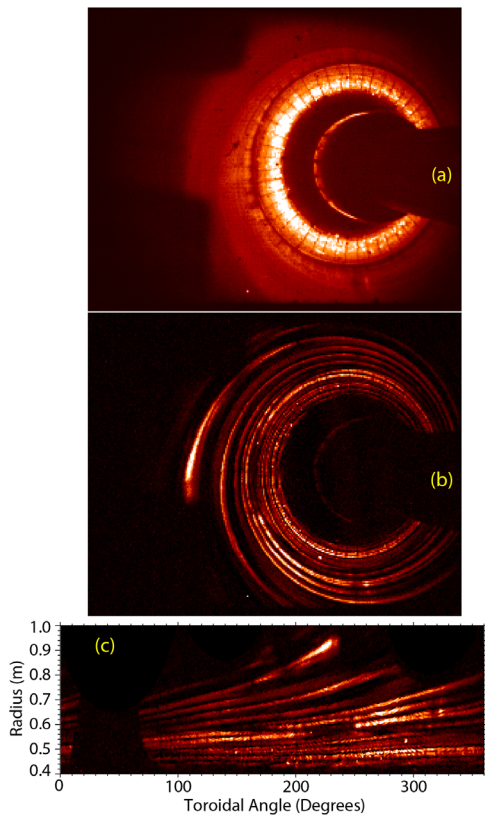
Figure 4. Images of the lower divertor in neutral lithium emission: (*a*) average over 1 ms, (*b*) single frame (9 μs) after moving minimum subtraction, (*c*) image in (*b*) plotted as a function of toroidal angle and divertor radius.

for Li I emission, sampled at different divertor radii and evaluated over 150 ms during the current flattop. The positive skewness of the PDF increases moving from the separatrix (black) to the far SOL (blue). Skewness and kurtosis are plotted in figure 6(*b*), sampled at three different divertor radii. Skewness and kurtosis are evaluated over 5 ms intervals and collected for 150 ms interval during the current flattop. Skewness and kurtosis increase radially and are overall consistent with the expectations for a Gamma-distributed quantity (i.e. quadratic dependence of kurtosis on skewness). The dependence of kurtosis on skewness for a Gamma distribution is overlaid in blue in figure 6(*b*).

Fluctuations in neutral lithium emission can be interpreted as representative of n_e fluctuations. Fluctuations in divertor Li I emission are compared with ion saturation current I_{sat} fluctuations measured by the divertor Langmuir probes. In figure 7(*a*), time histories from a pixel at the probe location (red) and I_{sat} (black) from the corresponding Langmuir probe (at $R_{div} = 0.70$ m) are shown after mean subtraction and normalization by the standard deviation. Cross correlation between the two time histories is shown in figure 7(*b*) as a function of delay. The cross correlation peaks at zero delay with a correlation of 0.75. While the Li I emission and I_{sat} time histories agree in terms of normalized fluctuations, the I_{sat} absolute fluctuation level is 2–3 times larger. This difference is possibly due to the smaller probe radial size (which therefore is able to sample smaller scale fluctuations) and
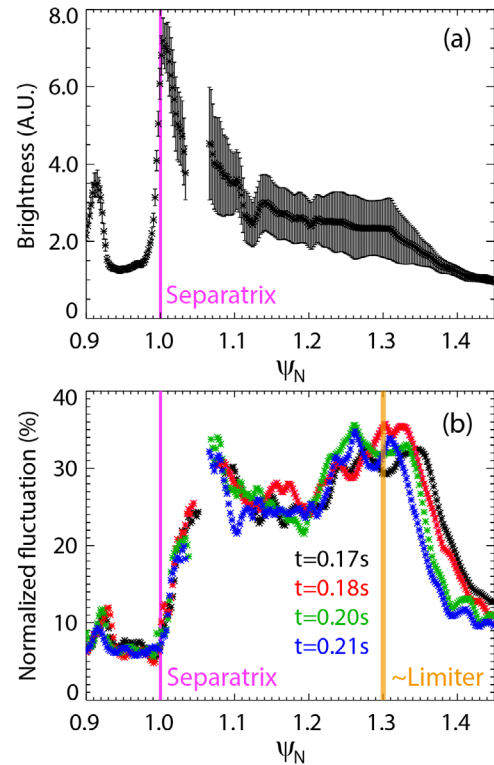
Figure 5. (*a*) Divertor neutral lithium emission as a function of ψ_N, (*b*) normalized divertor fluctuation level (standard deviation/mean) as a function of ψ_N over the same time interval for discharge 141754. The coaxial helicity injection gap in the divertor prevents imaging in the region around $\psi_N \sim 1.05$ at this time.
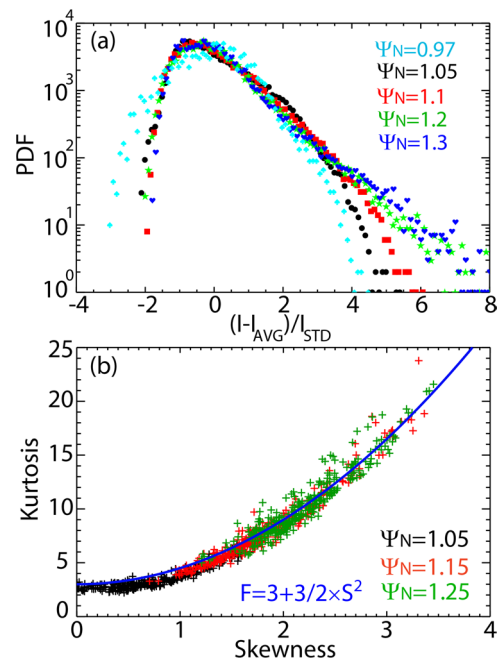
Figure 6. (*a*) Probability density function for Li I emission at different divertor radii, (*b*) kurtosis versus skewness for Li I emission. Overlaid in blue is the expectation for a gamma distributed quantity.

to the non-linearity in the Li I response to n_e fluctuations resulting from the inverse dependence of the photon emission coefficient on n_e [46].
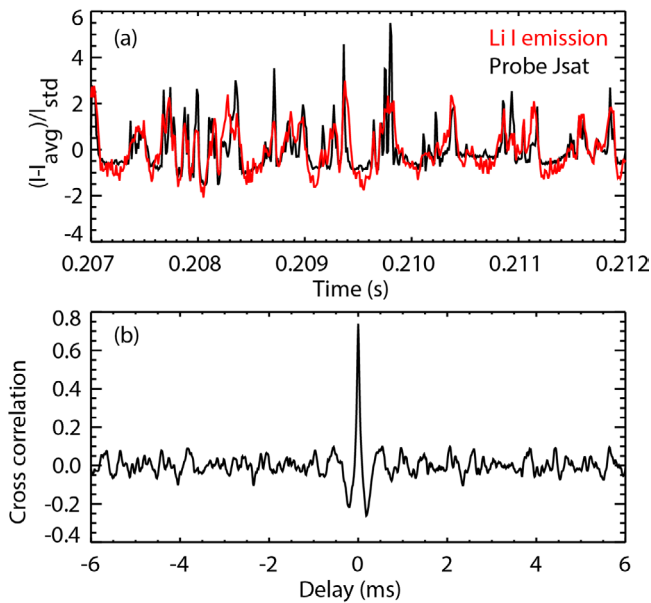
Figure 7. (*a*) Time history of I_{sat} from a divertor probe (black) and Li I emission from a pixel at the probe location (red) normalized by standard deviation. (*b*) Cross correlation between the two signals as a function of delay.

5. Midplane SOL turbulence characteristics

Midplane SOL turbulence properties have been extensively studied in NSTX via GPI [6, 47, 48] and Langmuir probes [49]. This section describes turbulence scale lengths and turbulence propagation velocities in ohmic L-mode discharges inferred from zero delay and time-delayed 2D cross correlations. Correlation scale lengths and turbulence velocities in these discharges are consistent with those presented in similar types of discharges in [6]. The correlation scale lengths correspond to a poloidal size scaling $k_{pol}\rho_s \sim 0.1$, not dissimilar to what is observed in other devices. The same reference also discusses the relation of turbulence scale lengths and velocities derived from cross correlation functions to typical blob size and velocity distributions.

Representative edge profiles of midplane T_e (black) and n_e, measured by MPTS, are plotted in figure 8 for one of the discharges in consideration (141754) at the time of the GPI gas puff. In order to derive blob parameters that will be used in section 8 (collisionality and normalized blob size [1]), spline fits to the Thomson scattering profiles (purple and cyan lines, respectively) are calculated. A close-up of the separatrix region is shown in the figure inset.

Turbulence scale lengths were inferred from the 2D cross correlation functions in five repeated ohmic L-mode discharges. 2D cross correlation functions from the NSTX GPI data are extensively described in [48]. In order to compare midplane and divertor scale lengths, the GPI data was low pass-filtered in frequency to the bandwidth of the divertor camera. Typical scale lengths were only marginally affected (increased by $\sim$10%) by the reduced bandwidth. For each discharge and at each radial location, cross correlations were calculated between the time history of a single pixel
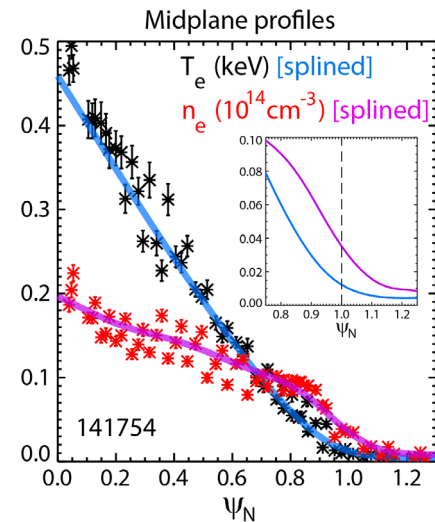
Figure 8. T_e (black) and n_e (red) profiles as a function of ψ_N. The spline fits used for derivation of blob parameters are overlaid (cyan and purple, respectively). A close up of the separatrix region is shown in the inset.

and those of every other pixel in the image over 10 ms at five different poloidal locations on the same flux surface (i.e. elevations). An example of midplane 2D cross correlation functions evaluated from the GPI data and projected in the (R, Z) plane is shown in figure 9. In figure 9, cross correlations are evaluated at three different poloidal locations on the same flux surface ($\psi_N = 1.08$ in black) and overlaid to the same NSTX equilibrium reconstruction. The separatrix is shown in red and the GPI field of view is shown in blue. Origin points of the cross correlations are shown with a blue symbol.

The radial and poloidal correlation lengths (L_{rad} and L_{pol}) were estimated from the full width at half maximum of the 2D correlation function interpolated onto radial and poloidal (binormal) coordinates. Figure 10(*a*) shows the radial (red) and poloidal (black) correlation lengths as a function of radius. Each curve represents a different discharge and the error bars for each discharge were estimated from the standard deviation of the correlation lengths evaluated at different elevations. L_{pol} were on the order of 6–7 cm and L_{rad} were on the order of 4 cm. Both scale lengths were approximately constant radially, with a decrease in the far SOL.

The poloidal and radial turbulence velocities (v_{pol} and v_{rad}) were calculated, using time delayed cross correlations, from the linear fit of the radial and poloidal location of the centroid of the cross correlation function over a $\pm 20\,\mu s$ delay. Positive radial velocities were observed across the entire radial profile between 0.3 and 1.0 km s^{-1}. Poloidal velocities were upward in the core (electron diamagnetic direction) and downward in the SOL between 1 and 3 km s^{-1}.

Comparing figures 5(*b*) and 10 we can see that the region characterized by a reduced fluctuation level in the divertor ($\psi_N \sim 1.0$–1.08), corresponds to the region with a relatively low radial turbulence velocity and the largest (negative) poloidal velocity. No changes are observed over this region in the turbulence scale lengths.
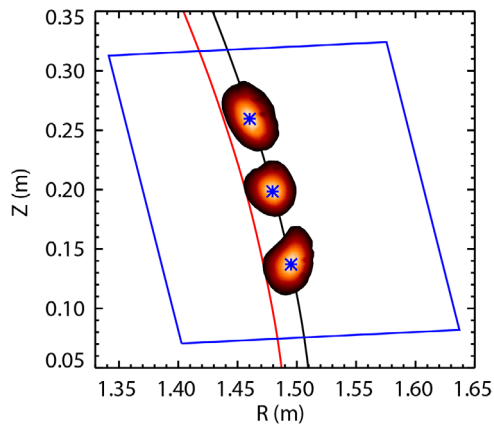
Figure 9. 2D cross correlation functions from the GPI data evaluated at three different poloidal locations and overlaid in the same plot. The filled contours represents correlation values between 0.5 and 1. The origin points of the cross correlations are shown with a blue symbol.

6. Comparison of midplane and divertor turbulence scale lengths and motion

In this section, divertor turbulence radial/poloidal correlation lengths and propagation velocities are derived from zero delay and time-delayed 2D cross correlations in ohmic L-mode discharges. Correlation scale lengths and turbulence velocities are compared with the corresponding quantities at midplane (presented in section 5) to investigate the extent of turbulence connection.

Divertor 2D cross correlation functions are calculated from the cross correlation of the time history of a single pixel in images like figure 4(*b*) with every other pixel in the image over 10 ms. For each discharge and divertor radius, starting pixels at different toroidal locations are used to estimate variation in the derived scale lengths and velocities. An example of a 2D divertor correlation function is shown in figure 11(*a*) as a function of toroidal angle and divertor radius. The 2D correlation map appears as a spiral wrapping around the axisymmetric outer strike point. The correlation extends over more than one toroidal turn. While small negative correlations are observed next to the positively correlated region (with correlation up to −0.2), no additional positively correlated regions are observed.

In order to compare divertor turbulence scale lengths and propagation velocities to the radial and poloidal quantities derived at midplane in section 5, we can apply what was discussed in section 3. The radial divertor correlation function is calculated evaluating the 2D correlation map along the spiral intersecting the divertor target plate (shown in figure 11(*a*) with blue dotted lines) and projecting it onto the divertor radial coordinate. The divertor radial coordinate is then mapped upstream to the corresponding radial coordinate within the GPI field of view enabling the direct comparison with the midplane radial correlation function. The toroidal divertor correlation function is calculated evaluating the 2D correlation map at a fixed radius (see solid blue line in figure 11(*a*)). The poloidal divertor correlation function is then derived projecting the toroidal correlation function onto
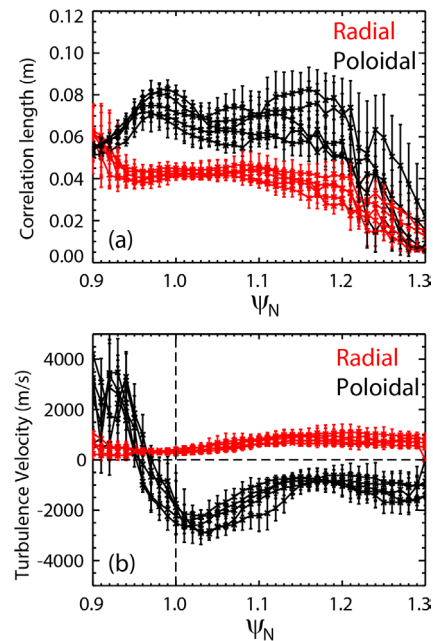
Figure 10. (*a*) Midplane poloidal (black) and radial (red) correlation lengths as a function of ψ_N. (*b*) Midplane poloidal (black) and radial (red) turbulence propagation velocity as a function of ψ_N.

the poloidal (binormal) coordinate at midplane assuming field aligned fluctuations. The radial (toroidal) divertor correlation function projected in this way is plotted in figures 11(*b*) and (*c*) as a function of divertor radius (toroidal angle).

Radial correlation functions at the divertor target and at midplane are plotted in figure 12. In comparing midplane and divertor radial correlation functions it should be noted that while midplane structures can span inside and outside the separatrix, divertor radial correlation functions are limited to the SOL common flux region, i.e. to radii larger than the LCFS. For origin points of the cross correlation located in the far SOL (figure 12(*a*)), divertor (black) and midplane (red) radial correlation functions are comparable. For origin points approaching the separatrix (figure 12(*b*)), narrower radial correlation functions (only considering the profile in the SOL side) are observed in the divertor region.

Radial profiles of the divertor ($L_{rad-div}$) and midplane (L_{rad}) radial correlation lengths evaluated from the half width at half maximum of the radial correlation function (in the SOL side) are plotted in figure 13(*a*). Good agreement is observed throughout the far SOL while a shorter radial correlation length is observed approaching the separatrix for $\psi_N \leqslant 1.1$. It should be noted that this is the same region over which a decrease in divertor fluctuation level was observed. Radial profiles of the divertor ($L_{pol-div}$) and midplane (L_{pol}) poloidal correlation lengths evaluated from the full width at half maximum of the poloidal correlation function are plotted in figure 13(*b*). $L_{pol-div}$ were a factor of ∼2–3 times larger than the corresponding midplane quantity across the entire radial profile. This can be schematically understood as if the ribbons stretched by flux expansion and magnetic shear were larger than field line mapping would imply. The reason for this discrepancy is not currently understood and could be
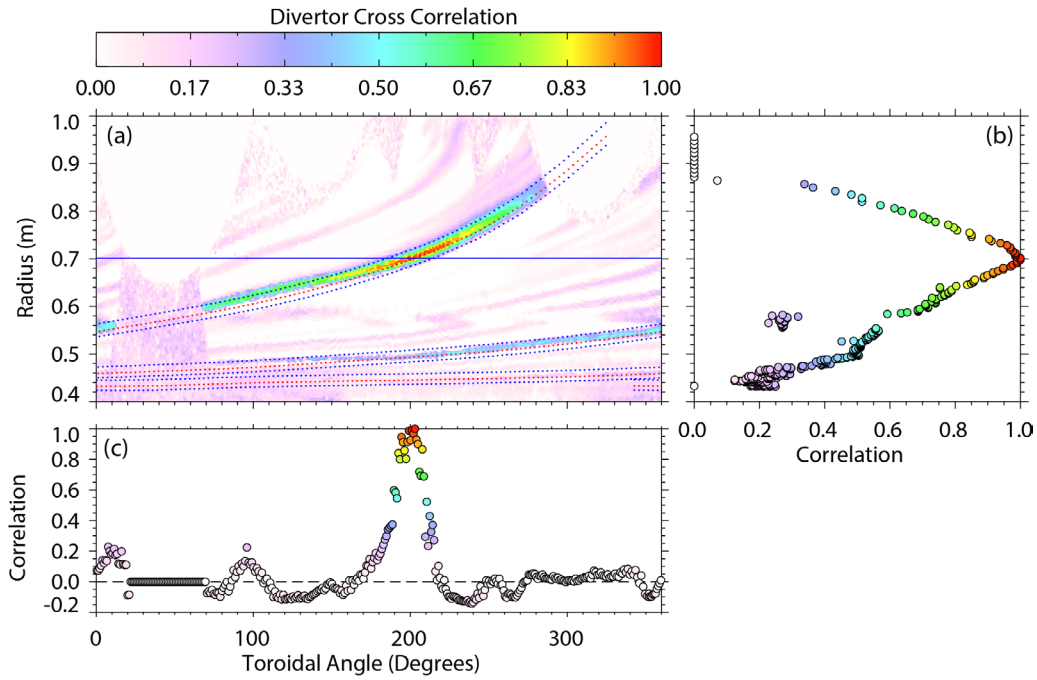
Figure 11. (*a*) 2D divertor cross correlation function plotted versus toroidal angle and divertor radius. Divertor radial (*b*) and toroidal (*c*) correlation functions obtained from the projection of the 2D cross correlation function. Each point in the correlation functions in (*b*) and (*c*) is color-coded to match the color scale in the 2D correlation map in (*a*).
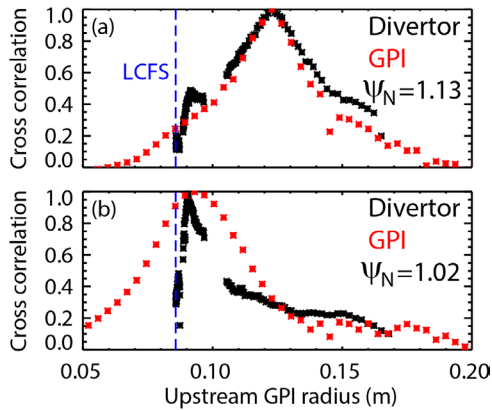
Figure 12. Divertor (black) and midplane (red) radial correlation functions evaluated in the far SOL (*a*) and in the proximity of the separatrix (*b*).

due to diffusion across the filament ribbon. The effect of filament poloidal motion over a finite camera integration time is small compared to the measured poloidal correlation lengths. The derivation of $L_{\rm pol-div}$ for $\psi_{\rm N} \leqslant 1.1$ is complicated by the smaller pitch of the target spiral.

Divertor turbulence velocities were derived from time delayed cross correlations. An example of 2D divertor cross correlation functions at different delays is shown in figure 14(*a*) as a function of toroidal angle and divertor radius ($t = -40 \mu$ s in blue, $t = 40 \mu$s in red). Radial and toroidal correlation functions are shown for the two delays in figures 14(*b*) and (*c*), respectively, together with the correlation function at zero delay (white). Radial motion was inferred from the motion of the peak of the radial cross correlation function as a function of delay. Poloidal motion was inferred from the toroidal
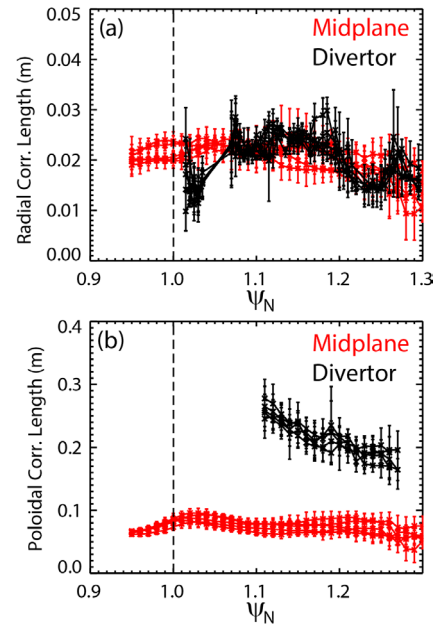
Figure 13. Divertor (black) and midplane (red) radial (*a*) and poloidal (*b*) correlation lengths as a function of $\psi_{\rm N}$.

translation of the spiral, mapped to a poloidal motion in the GPI plane.

Radial profiles of the divertor ($v_{\rm rad-div}$) and midplane ($v_{\rm rad}$) radial turbulence velocities are plotted in figure 15(*a*). Radial profiles of the divertor ($v_{\rm pol-div}$) and midplane ($v_{\rm pol}$) poloidal turbulence velocities are plotted in figure 15(*b*). Good agreement is observed at every radius for poloidal velocities. Radial velocities, while generally consistent between midplane and
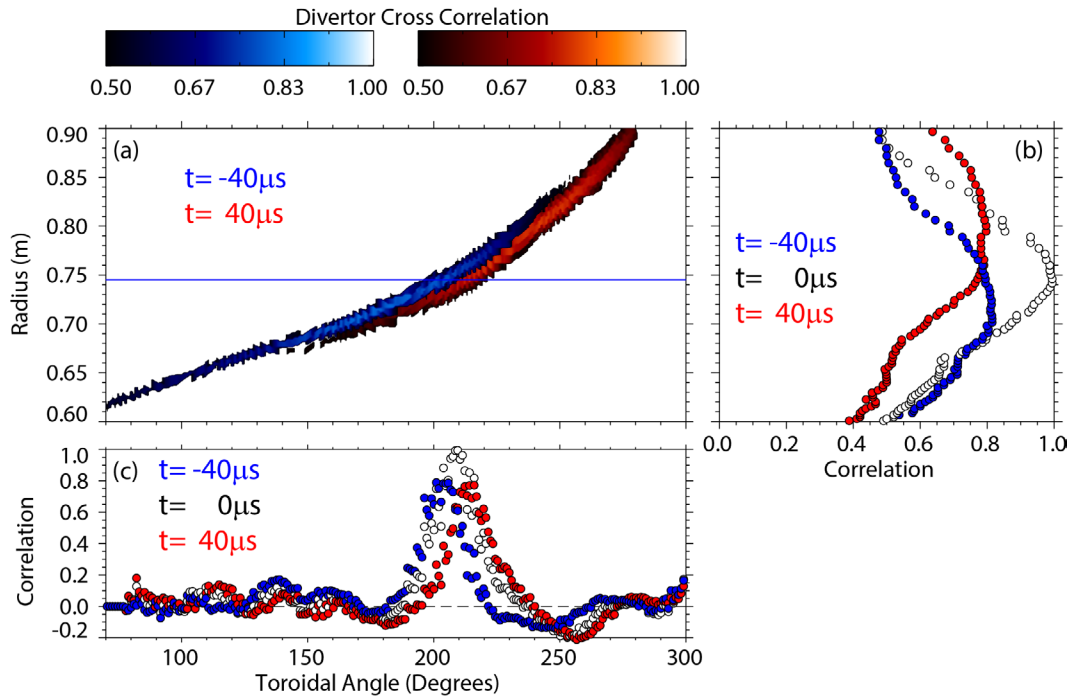
Figure 14. (*a*) 2D Divertor cross correlation function plotted versus toroidal angle and divertor radius for a delay of −40 μs (blue) and of 40 μs (red). Divertor radial (*b*) and toroidal (*c*) correlation functions obtained from the projection of the 2D cross correlation function for −40 μs (blue), 0 μs (white) and 40 μs (red) delay.
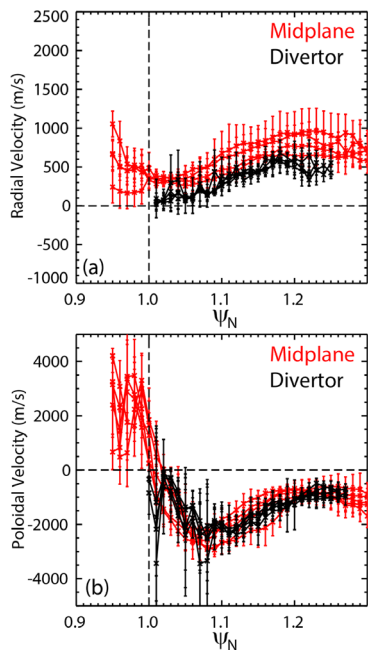
Figure 15. Divertor (black) and midplane (red) radial (*a*) and poloidal (*b*) turbulence velocity as a function of ψ_N.

divertor, are systematically lower in the divertor. A larger reduction of the radial velocity in the proximity of the separatrix is observed. It should be noted that in order for the poloidal velocity profile to match upstream and downstream a shift in the midplane normalized flux coordinate of 0.05 was necessary. This corresponded to a shift in separatrix position ∼1 cm which can be on the order of the uncertainties of the equilibrium reconstruction. The same shift was applied consistently in figures 15 and 13.
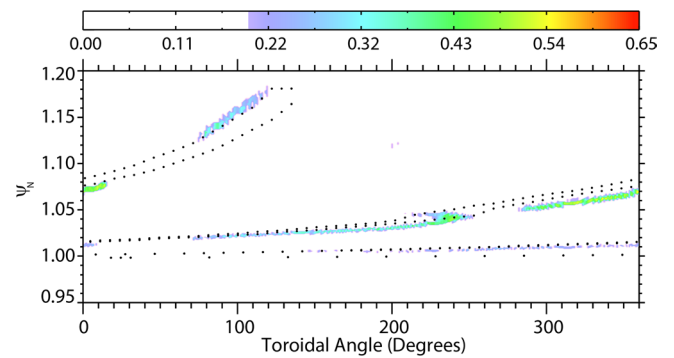
Figure 16. 2D cross correlation between time histories of one pixel within the GPI view and every pixel in the divertor view as a function of toroidal angle and radius. The divertor region mapping to the GPI field of view is overlaid with black dashed lines.

7. Midplane and divertor plate turbulence cross correlation

The connection between midplane and divertor was further investigated via cross correlation between time series of the GPI and divertor fast cameras, similarly to what was done in [18]. For each pixel in the GPI view, the cross correlation at zero delay between the time series of that pixel and that of every pixel in the divertor view was evaluated (for a total of $64 \times 80 \times 256 \times 208$ cross correlations).

An example of the 2D divertor correlation map with a single GPI pixel is shown in figure 16 as a function of toroidal angle and ψ_N. In the contour plot, regions with correlation below 0.2 were suppressed for clarity. As expected, the correlation region is of spiral shape. Overlaid with a dotted line is the envelope of the region that magnetically maps to the
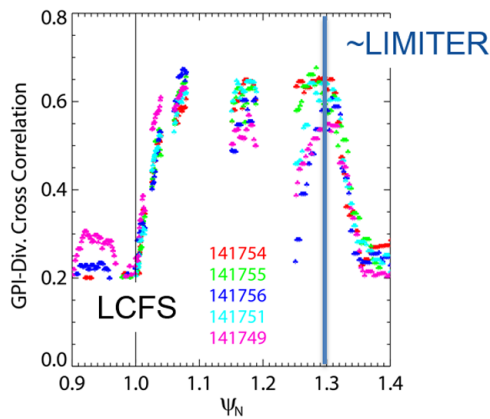
Figure 17. Maximum value of cross correlation between GPI and divertor imaging for each divertor radius, plotted as a function of ψ_N for 5 different discharges.
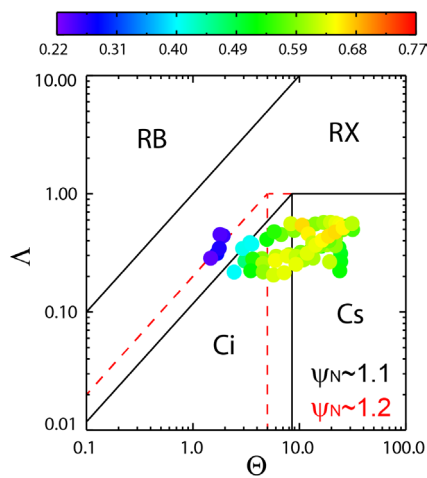
Figure 18. Cross correlation between midplane and divertor turbulence plotted as a function of normalized blob size parameter Θ and normalized collisionality Λ for the five discharges in consideration. The color of each data point represents the value of the cross correlation. Boundaries of the blob regimes are overlaid.

(R, Z) coordinates of GPI field of view at the toroidal location of the gas manifold. The divertor region which is positively correlated with GPI is the region that is magnetically connected to it. Deviations between the correlation shape and the shape of the mapped region are however observed and could be due to imperfect equilibrium reconstruction, non-perfectly field aligned fluctuations or the accuracy of the spatial calibration. This is left for future investigation.

For each divertor radial location, the maximum cross correlation with every pixel in the GPI view was evaluated. The midplane/divertor correlation was then plotted as a function of normalized poloidal flux (evaluated in the divertor) for the five discharges in consideration in figure 17. Reproducible results were obtained in all 5 discharges in consideration. Large correlations, up to 0.7, are observed in the far SOL. This is consistent with previous observations in H-mode discharges in NSTX [18]. A reduction in the correlation is observed on both sides of this region. At larger radii, correlation is lost beyond the radii that magnetically map to the LFS limiter, as expected. Correlation is also progressively decreasing approaching the separatrix starting at ψ_N of 1.08. The regions with missing
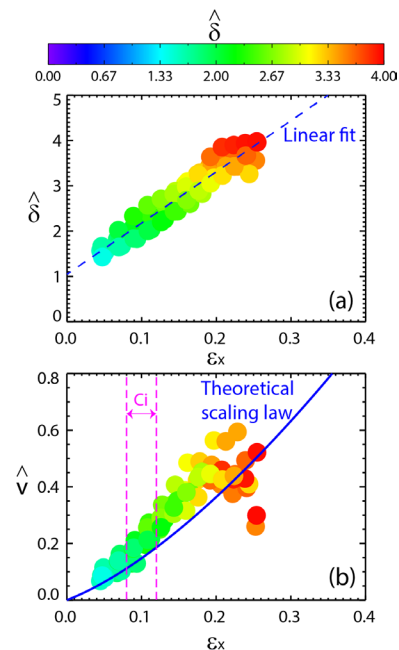
Figure 19. (*a*) Experimental values of normalized blob size $\hat{\delta}$ as a function of ϵ_x, a proxy for a radial coordinate from the separatrix. A best fit straight line for the functional dependence is overlaid. (*b*) Experimental values of normalized radial blob velocity $\hat{v}$ as a function of ϵ_x. The overlaid curve is the theoretical scaling law for the C_i regime. See the main text for a detailed explanation. In both parts (*a*) and (*b*) the color of each data point represents the value of normalized blob size.

data in the plot at $\psi_N \sim 1.05, 1.1$ and 1.23 are due to the presence of the center stack and the coaxial helicity injection gap that prevent the near-surface imaging of the divertor fluctuations. Overall, the region with large fluctuations in figure 5(*b*) coincides with the region where fluctuations are correlated with midplane turbulence.

8. Discussion

The connection between midplane turbulence and the divertor target was investigated for NSTX ohmic L-mode discharges by comparing turbulence scale lengths and propagation velocities and analyzing turbulence correlation. In the far SOL, the region between $\psi_N = 1.1$–1.3 was characterized by the largest divertor fluctuation level (see figure 5). In this region, radial turbulence correlation lengths and radial and poloidal propagation velocities in the divertor were similar to those measured at the LFS midplane (figures 13 and 15). This region also had the largest correlation with midplane turbulence (figure 17). For $\psi_N \leqslant 1.1$, both the divertor fluctuation level and the correlation with midplane turbulence progressively decreased indicating a disconnection of midplane turbulence from the turbulence measured at the divertor plate near the separatrix. This radial region showing turbulence disconnection coincided with the minimum in the turbulence radial velocity and the largest negative poloidal velocity in the edge. Over the same region, divertor radial correlation lengths were significantly shorter than those measured at midplane. It should be noted that throughout the region with progressively decreasing

correlation, divertor 2D cross correlation functions still had the typical spiral shape consistent with the divertor extension of midplane blobs. These observations are consistent with expectations of X-point disconnection of midplane filaments.

Divertor density fluctuations are a manifestation of divertor potential fluctuations coupled to midplane potential fluctuations. Experimentally, correlation between midplane and divertor density fluctuations are largest at 'zero' delay [18]. 'Zero' in this case meaning within 1 camera frame ($\leqslant 10 \ \mu$s). The time scale for ion propagation from midplane to the divertor is on the order of $100 \ \mu$s ($L_\parallel/c_s$). The electrons set up the local potentials on the field line on short time scales $\sim 1 \ \mu$s [50], which cause the density to fluctuate in synch at midplane and divertor due to the local $E \times B$ and local density gradient. The ions do not have time to propagate along field lines from midplane to the divertor in one fluctuation period. In this sense the measured density correlation is relevant with respect to the electrical connection of the perturbation to the divertor.

The experimental observations of turbulence disconnection were compared with predictions from the electrostatic two-region blob model described in [1]. The skewed PDFs in figure 6(*a*) show that the measured turbulence is intermittent and has the statistical characteristics expected from blob-dominated turbulence [51]. Further, [51] relates turbulence linear properties such as wavenumber and growth rate to blob size and propagation velocity via the *blob correspondence principle*. The blob regimes found in [1] should then have broad qualitative applicability to turbulent fluctuations whether or not they meet a more narrow definition of a coherent blob structure, warranting the application to the correlation analysis in this paper.

The two region model [1] is based on two sets of continuity and vorticity equations solved in the electrostatic limit at midplane and divertor leg. Following [51, 54], the two-region model defines different blob regimes (connected and disconnected from the divertor region): the sheath-connected regime C_s where filaments are connected to the divertor plate and the parallel current driven by midplane curvature is limited by sheath resistivity, the ideal-interchange regime C_i where the midplane curvature drive is balanced by perpendicular ion polarization currents enhanced by the X-point geometry, the resistive X-point regime *RX* (disconnected) where parallel currents are limited by divertor plasma resistivity and the resistive balooning limit *RB* (disconnected) where the midplane drive is balanced by inertia at midplane.

These regimes can be identified in a blob regime diagram as a function of a collisionality parameter Λ and a blob size parameter Θ. The collisionality parameter Λ is defined as $\frac{\nu_{ei} L_\parallel}{\Omega_e \rho_s}$. The blob size parameter Θ is defined as $\hat{\delta}^{5/2}$ where the dimensionless blob size $\hat{\delta}$ is obtained normalizing the blob size δ_b by the characteristic blob scale $\delta_* = \rho_s \left(\frac{L_\parallel^2}{\rho_s R} \right)^{1/5}$. In these equations, $L_\parallel$ is the midplane to target connection length, ν_{ei} is the electron–ion collision frequency, ρ_s is the sound Larmor radius, R is the major radius, and Ω_e is the electron gyrofrequency.

Another quantity that needs to be introduced to define the boundaries in the blob diagram is the X-point magnetic fanning parameter ϵ_x. The exact calculation for ϵ_x can be found in [1]. In this paper, a proxy for ϵ_x is used, obtained evaluating the ratio of $B_{tor}/(RB_{pol})$ at midplane and at the divertor. In the two region model, ϵ_x is defined as the ratio of k_{perp} (composed of k_θ and k_ψ) at the midplane to k_{perp} at the X-point where k_{perp} is proportional to the inverse minor radius of an elliptical field-aligned blob-filament, measuring the stretching of a flux tube. Although integrated magnetic shear affects the flux surface distortion particularly between the X-point and target, ϵ_x is well approximated by the flux surface expansion effect and is roughly proportional to the ratio RB_{pol} at the midplane to RB_{pol} at the X-point, obtained neglecting k_ψ and taking the ratio of k_θ at midplane and divertor. This is zero at the separatrix and increases approximately linearly as one moves into the SOL and will eventually saturate far enough in the SOL.

In the blob diagram in figure 18, as a function of Λ and Θ, the C_s regime is bound by $\Lambda \leqslant 1$ and $\Theta \geqslant 1/\epsilon_x$ (~ 10 here), the C_i regime is bound by $\Lambda \leqslant \epsilon_x \Theta$ and $\Theta \leqslant 1/\epsilon_x$, the *RB* regime is found for $\Lambda \geqslant \Theta$ and the *RX* regime is found in the region between the C_s–C_i regimes and the *RB* regime. Since ϵ_x varies radially, in the regime plot in figure 18 the boundaries are shown using the values for ϵ_x at the region where filament disconnection begins to be observed experimentally (i.e. $\psi_N = 1.1$). The boundaries for $\psi_N = 1.2$ are also overlaid with dashed red lines.

Experimental values of the turbulence correlation between midplane and divertor are plotted in the blob regime diagram as a function of Λ and Θ for five repeated L-mode discharges in figure 18. For each discharge, midplane to divertor target correlation (see figure 17) and blob parameters were evaluated. At each radial location, local midplane T_e, n_e, magnetic field, midplane to target connection length (calculated from the EFIT02 reconstruction) and blob size (inferred from the HWHM of the poloidal correlation function) were used to derive the blob parameters. In the far SOL, blobs are in the C_s regime. Moving from the far SOL to the separatrix, the blob regime changed due to a reduction in normalized blob size with an approximately unchanged normalized collisionality ($\Lambda \sim 0.2$–0.6), therefore moving from the C_s to the C_i and towards the *RX* regime. In the regime plot, the color of each experimental point corresponds to the measured cross correlation (blue corresponding to a disconnected blob and orange corresponding to a connected blob). Uncertainties in plasma parameters in the far SOL represent the largest uncertainty in the derivation of the blob parameters, but the spread of results obtained in repeated discharges can give an idea of the actual uncertainty. Blob disconnection is observed transitioning from the C_s regime to the C_i and *RX* regimes, supporting the role of X-point geometry and collisionality for the disconnection of midplane instabilities from the divertor target. It should also be noted that over the same region (between $\psi_N \sim 1.1$ and $\psi_N \sim 1.01$) the midplane to divertor target connection length approximately doubles (from 5 m to 10 m).

The lower blob v_{rad} near the separatrix is expected from the model described in [1]. Blob disconnection from the

divertor can cause changes in the blob radial velocity, due to changes in effective resistivity of the blob circuit. As discussed in [51], the X-point geometry promotes short circuiting of the polarization charge that drives the blob radial velocity. The stretching of the flux tubes in the proximity of the X-point, at constant collisionality, decreases the effective resistivity of the filament current loop and increases its inertia, lowering the filament radial velocity. In figure 19(*a*), it is shown that the experimental values of normalized blob size $\hat{\delta}$ (inferred from the HWHM of the poloidal correlation function) have a nearly offset linear dependence on ϵ_x, which, as discussed earlier, is itself approximately a linear function of the distance from the separatrix and can thus be a proxy for a radial coordinate. Given the approximately radially constant poloidal correlation length, the radial variation in normalized blob size is determined by changes in background plasma and magnetic parameters. In figure 19(*b*), the experimental values of normalized radial blob velocity $\hat{v} = v_{\rm rad}/v_*$ (where $v_* = c_s(\delta_*/R)^{1/2}$ and c_s is the sound speed) are shown as a function of ϵ_x. The overlaid curve is the theoretical scaling law for the C_i regime. In the C_i regime the theoretically expected scaling from the two region model is $\hat{v} = \epsilon_x\hat{\delta}^{1/2}$. To obtain the theoretical curve overlaid in figure 19(*b*), the best fit linear relationship for $\hat{\delta}(\epsilon_x)$ obtained from figure 19(*a*) is employed. Similar agreement for velocity scaling in different blob regimes was also recently found in TCV from Langmuir probe measurements [52].

There are no free parameters in making this comparison, but several caveats should be noted. The C_i regime for this dataset strictly applies only over the small range $0.08 \leqslant \epsilon_x \leqslant 0.12$ where the lower boundary with the *RX* regime is determined by the condition $\epsilon_x\hat{\delta}^{5/2} = \Lambda$, with $\Lambda = 0.4$ here, while the upper boundary with the C_s regime is determined by the condition $\epsilon_x\hat{\delta}^{5/2} = 1$. Nevertheless most of the data for $\epsilon_x \leqslant 0.2$ in figure 19(*b*) seems to follow the C_i scaling rather well. It should be kept in mind that the two-region model of [1] is rather crude in its representation of X-point geometry, and while useful for understanding blob velocity scaling laws, it is not expected to give accurate order-unity coefficients in those scaling laws or in the regime boundaries. It may also be that the determination of the C_i boundaries are uncertain in part due to the uncertainty in mapping the data to ϵ_x, as well as the uncertainty in the temperature used in the normalization to obtain $\hat{\delta}$. The data in figure 19(*b*) for $\epsilon_x > 0.2$ shows a distinct break from the C_i scaling. This is consistent with a transition from C_i scaling to C_s scaling for sufficiently large δ. In the C_s regime the scaling from the two-region model is $\hat{v} = 1/\hat{\delta}^2$. Since $\hat{\delta}$ increases with ϵ_x the C_s scaling implies that $\hat{v}$ should decrease with ϵ_x beyond the C_i–C_s transition, as observed in figure 19(*b*). Finally, it should be noted (see [51]) that the effect on $v_{\rm rad}$ due to X-point geometry is opposite to that resulting from increased collisionality at fixed X-point fanning. The latter is predicted to cause an increase in the

blob radial velocity and has been associated with shoulder formation mechanisms [29].

9. Conclusions

Disconnection of SOL turbulence between the outer midplane and the divertor target was characterized in ohmic L-mode plasmas in the National Spherical Torus Experiment (NSTX). Divertor fluctuations due to midplane turbulence were studied in NSTX via fast camera imaging of their helical intersection with the divertor plate. Divertor radial turbulence scale lengths as well as radial and poloidal turbulence propagation velocities were comparable to those on the LFS midplane. In the region approaching the separatrix, divertor fluctuation levels gradually decreased together with a decrease in the correlation between midplane and divertor turbulence and a decrease in the divertor radial correlation lengths. These observations were consistent with disconnection of midplane turbulence due to X-point magnetic shear effects.

The reduction in correlation was in agreement with an electrostatic two-region blob model [1] with perpendicular ion polarization currents due to X-point geometry causing filament disconnection. The measured reduction in turbulence radial velocity was also expected from the two-region model due to a reduction in the effective resistivity of the blob circuit.

Future work should focus on whether the existing NSTX database can cover also other regime transitions in the blob diagram in terms of changes in divertor connectivity. Theoretically, as discussed earlier in the paper, connection to the divertor target plate would impact the blob velocity. If blob radial motion contributes to the cross-field spreading of the n_e and T_e profiles, then the parallel connection could be affecting the SOL heath flux width. Furthermore, there is experimental evidence of a dependence of the heat flux width on divertor leg length in TCV [53], indicating a possible importance of divertor transport which could be modified by connection physics. This work would also benefit from a better radial divertor coverage of Langmuir probes (to provide collisionality changes in the divertor region) which is expected in the upcoming NSTX-Upgrade device.

ORCID iDs

F. Scotti ⓘ https://orcid.org/0000-0002-0196-9919
S. Zweben ⓘ https://orcid.org/0000-0002-1738-0586
J. Myra ⓘ https://orcid.org/0000-0001-5939-8429
V. Soukhanovskii ⓘ https://orcid.org/0000-0001-5519-0145

References

[1] Myra J.R., Russell D.A. and D'Ippolito D.A. 2006 *Phys. Plasmas* **13** 112502
[2] Eich T. *et al* (ASDEX Upgrade Team and JET EFDA Contributors) 2013 *Nuclear Fusion* **53** 093031
[3] Goldston R. 2012 *Nucl. Fusion* **52** 013009
[4] Stangeby P. 2011 *J. Nucl. Mater.* **415** S278–83
[5] Zweben S. *et al* (The NSTX Team) 2004 *Nucl. Fusion* **44** 134
[6] Zweben S. *et al* 2015 *Nucl. Fusion* **55** 093035
[7] Kirk A. *et al* (The MAST Team) 2006 *Plasma Phys. Control. Fusion* **48** B433–41
[8] Ayed N.B., Kirk A., Dudson B., Tallents S., Vann R.G.L. and and Wilson H.R. 2009 *Plasma Phys. Control. Fusion* **51** 035016
[9] Boedo J. 2009 *J. Nucl. Mater.* **390–1** 29–37
[10] Rudakov D.L. *et al* 2002 *Plasma Phys. Control. Fusion* **44** 717–31
[11] Terry J.L. *et al* 2003 *Phys. Plasmas* **10** 1739–47
[12] Garcia O.E., Horacek J., Pitts R.A., Nielsen A.H., Fundamenski W., Graves J.P., Naulin V. and Rasmussen J.J. 2006 *Plasma Phys. Control. Fusion* **48** L1
[13] Müller H. *et al* 2011 *Nucl. Fusion* **51** 073023
[14] Tanaka H., Ohno N., Asakura N., Tsuji Y., Kawashima H., Takamura S., Uesugi Y. and The JT-60U Team 2009 *Nucl. Fusion* **49** 065017
[15] Boedo J.A. *et al* 2001 *Phys. Plasmas* **8** 4826–33
[16] Antar G.Y., Counsell G., Ahn J.W., Yang Y., Price M., Tabasso A. and Kirk A. 2005 *Phys. Plasmas* **12** 032506
[17] Müller S.H. *et al* 2014 *Phys. Plasmas* **21** 042301
[18] Maqueda R., Stotler D. and The NSTX Team 2010 *Nucl. Fusion* **50** 075002
[19] Terry J., Zweben S., Umansky M., Cziegler I., Grulke O., LaBombard B. and Stotler D. 2009 *J. Nucl. Mater.* **390–1** 339–42
[20] Grulke O., Terry J., Cziegler I., LaBombard B. and Garcia O. 2014 *Nucl. Fusion* **54** 043012
[21] Cavalier J., Lemoine N., Brochard F., Weinzettl V., Seidl J., Silburn S., Tamain P., Dejarnac R., Adamek J. and Panek R. 2019 *Nucl. Fusion* **59** 056025
[22] Harrison J.R., Fishpool G.M., Thornton A.J., Walkden N.R. and The MAST Team 2015 *Phys. Plasmas* **22** 092508
[23] Terry J., Ballinger S., Brunner D., LaBombard B., White A. and Zweben S. 2017 *Nucl. Mater. Energy* **12** 989–93
[24] Scotti F., Zweben S., Soukhanovskii V., Baver D. and Myra J. 2018 *Nucl. Fusion* **58** 126028
[25] Walkden N., Harrison J., Silburn S., Farley T., Henderson S., Kirk A., Militello F., Thornton A. and The MAST Team 2017 *Nucl. Fusion* **57** 126028
[26] Avino F., Fasoli A., Furno I., Ricci P. and Theiler C. 2016 *Phys. Rev. Lett.* **116** 105001
[27] Myra J.R. and D'Ippolito D.A. 2005 *Phys. Plasmas* **12** 092511
[28] Farina D., Pozzoli R. and Ryutov D. 1993 *Nucl. Fusion* **33** 1315
[29] Carralero D. *et al* 2015 *Phys. Rev. Lett.* **115** 215002
[30] Wynn A. *et al* 2018 *Nucl. Fusion* **58** 056001
[31] Vianello N. *et al* 2017 *Nucl. Fusion* **57** 116014
[32] Baver D.A. and Myra J.R. 2019 *Phys. Plasmas* **26** 022505
[33] Umansky M.V., Rognlien T.D., Xu X.Q., Cohen R.H. and Nevins W.M. 2004 *Contrib. Plasma Phys.* **44** 182–7
[34] Zweben S.J., Terry J.L., Stotler D.P. and Maqueda R.J. 2017 *Rev. Sci. Instrum.* **88** 041101
[35] Scotti F., Roquemore A. and Soukhanovskii V. 2012 *Rev. Sci. Instrum.* **83** 10E532
[36] Kallman J., Jaworski M., Kaita R., Kugel H. and Gray T. 2010 *Rev. Sci. Instrum.* **81** 10E117
[37] Leblanc B., Diallo A., Labik G. and Stevens D. 2012 *Rev. Sci. Instrum.* **83** 10D527
[38] POVRAY 2008 Persistence of Vision Raytracer (www.povray.org/)
[39] Scotti F. *et al* 2015 *J. Nucl. Mater.* **463** 1165–8
[40] Kube R., Garcia O.E., Theodorsen A., Brunner D., Kuang A.Q., LaBombard B. and Terry J.L. 2018 *Plasma Phys. Control. Fusion* **60** 065002
[41] Garcia O., Kube R., Theodorsen A., Bak J.G., Hong S.H., Kim H.S., Pitts R. and The KSTAR Project Team 2017 *Nucl. Mater. Energy* **12** 36–43
[42] Garcia O., Horacek J. and Pitts R. 2015 *Nucl. Fusion* **55** 062002
[43] Labit B. *et al* 2007 *Plasma Phys. Control. Fusion* **49** B281–90
[44] Graves J.P., Horacek J., Pitts R.A. and Hopcraft K.I. 2005 *Plasma Phys. Control. Fusion* **47** L1–9
[45] Garcia O.E. 2012 *Phys. Rev. Lett.* **108** 265001
[46] Summers H.P. 2004 The ADAS User Manual, version 2.6 (www.adas.ac.uk)
[47] Zweben S.J. *et al* 2016 *Plasma Phys. Control. Fusion* **58** 044007
[48] Zweben S.J., Stotler D.P., Scotti F. and Myra J.R. 2017 *Phys. Plasmas* **24** 102509
[49] Boedo J.A. *et al* 2014 *Phys. Plasmas* **21** 042309
[50] Umansky M., Rognlien T. and Xu X. 2005 *J. Nucl. Mater.* **337–9** 266–70
[51] D'Ippolito D., Myra J. and Zweben S. 2011 *Phys. Plasmas* **18** 060501
[52] Tsui C.K. *et al* 2018 *Phys. Plasmas* **25** 072506
[53] Maurizio R., Elmore S., Fedorczak N., Gallo A., Reimerdes H., Labit B., Theiler C., Tsui C. and Vijvers W. 2017 *Nucl. Fusion* **58** 016052
[54] Krasheninnikov S.I., d'Ippolito D.A. and Myra J.R. 2008 *J. Plasma Phys.* **74** 679–717